



Reactant friendly hydrogen evolution interface based on di-anionic MoS₂ surface

Zhaoyan Luo^{1,2,5}, Hao Zhang^{3,5}, Yuqi Yang^{3,5}, Xian Wang^{1,2,5}, Yang Li^{1,2,5}, Zhao Jin¹, Zheng Jiang^{3,4}, Changpeng Liu¹, Wei Xing¹ & Junjie Ge¹

Engineering the reaction interface to preferentially attract reactants to inner Helmholtz plane is highly desirable for kinetic advancement of most electro-catalysis processes, including hydrogen evolution reaction (HER). This, however, has rarely been achieved due to the inherent complexity for precise surface manipulation down to molecule level. Here, we build a MoS₂ di-anionic surface with controlled molecular substitution of S sites by -OH. We confirm the -OH group endows the interface with reactant dragging functionality, through forming strong non-covalent hydrogen bonding to the reactants (hydronium ions or water). The well-conditioned surface, in conjunction with activated sulfur atoms (by heteroatom metal doping) as active sites, giving rise to up-to-date the lowest over potential and highest intrinsic activity among all the MoS₂ based catalysts. The di-anion surface created in this study, with atomic mixing of active sites and reactant dragging functionalities, represents a effective di-functional interface for boosted kinetic performance.

¹State Key Laboratory of Electroanalytical Chemistry, Jilin Province Key Laboratory of Low Carbon Chemical Power, Changchun Institute of Applied Chemistry, Chinese Academy of Sciences, 130022 Changchun, China. ²University of Science and Technology of China, 230026 Anhui, China. ³Shanghai Advanced Research Institute, Chinese Academy of Sciences, 201800 Shanghai, China. ⁴Shanghai Synchrotron Radiation Facility, Zhangjiang National Lab, Chinese Academy of Sciences, 201204 Shanghai, China. ⁵These authors contributed equally: Zhaoyan Luo, Hao Zhang, Yuqi Yang.

✉email: jiangzheng@sinap.ac.cn; gejj@ciac.ac.cn

The hydrogen production from electrochemical water splitting, which enables the energy cycling between electricity and hydrogen, constitutes the cornerstone of the sustainable hydrogen economy. Hydrogen evolution reaction (HER) electrocatalysts that are fast in kinetics, low in energy consumption, and cost-effective in nature were intensively searched, among which MoS₂ has emerged as a promising candidate^{1–3}. The overall kinetic performance (in Volmer-Heyrovsky mechanism) of the MoS₂ electrode at fixed potential (E) is shown in Eq. 1^{4,5} and is apparently governed by: first, the energetic interaction between atomic hydrogen and the surface site (ΔG_{H^*}); second, the reactant (hydronium ions in acid and water in alkaline medium) concentration. Most of the recent endeavors were paid on advancing the MoS₂ catalytic efficiency through the former, i.e., the orbital overlap and chemical interactions between adsorbates and the surface sites^{6,7}, including our recent work on Pd-doped MoS₂⁸. However, the latter reactant concentration part is rarely studied, which calls for extreme attention. Notably, this concentration is by no means the bulky value, but rather the one in the vicinity of the electrode. Therefore, it relies heavily on the property of the electrode materials at the interface and thereby partially determines the final catalytic behavior^{9,10}. For instance, an electrode can be simultaneously of optimized ΔG for intermediate species, meanwhile expressing poor reactivity due to the unfriendly interface (double layer) structure that pushing away or inhibit the movement of reactants¹¹.

$$j = - \frac{2Fk_2^0 [H^+]^{1-\alpha} \exp\left(\frac{-\alpha F E_{RHE} + (1-\beta)\Delta G_H}{RT}\right)}{1 + \frac{k_0^a}{k_1^a} \exp\left(\frac{F E_{RHE} + \Delta G_H}{RT}\right) + \frac{k_0^c}{k_1^c} \exp\left(\frac{\Delta G_H}{RT}\right)}, \quad (1)$$

For the HER reaction, water molecules/hydronium ions in bulky solution are attracting each other through the non-covalent hydrogen bonding, with stabilization energy at 20–40 kJ mol⁻¹. The lack of such bonding between the hydronium ions/water molecules and the electrode surface would hinder them from accessing the inner Helmholtz plane (IHP), if no additional interactions (such as the hydrogen under potential deposition at Pt surface) are formed^{11,12}. Therefore, a well-conditioned surface that preferentially attracts the hydronium ions/water molecules is essentially required for HER kinetic advancement. However, such interface engineering is largely neglected to date, thus leaving unpredictable values uncovered.

The oxygen-containing species can act as perfect ligands for surface engineering, under the consideration that these groups can form hydrogen bonding with hydronium ions/water molecules and attract these reactants to the surface. Previous literature have already revealed that the substitution of sulfur by oxygen species occur at certain circumstances. Specially, Levente Tapaszó et al.¹³ reported unambiguously that oxygen atoms can spontaneously incorporate into the basal plane of MoS₂ single layers through substitutional oxidation, when subjected to long-term ambient exposure. Alexander Weber-Bargioni et al.¹⁴ also identified the oxygen substitution on the sulfur sites in other monolayer transition metal dichalcogenides. However, it is noted that the oxidation of single layer basal plane already exhibits a high kinetic barriers of ~1.0 eV, thus leading to a slow oxidation kinetics with a timescale of months at room temperature. Harsh oxidation processes, on the contrary, overcome the kinetic barrier at the expense of over oxidation and destroying the original MoS₂ crystal lattice. Therefore, the controlled oxygen substitution is highly desirable. Meanwhile, introducing appropriate oxygen species (such as –OH) is highly important for interface engineering to preferentially attract the hydronium ions/water, however, to the best of our knowledge, this area hasn't been explored yet and therefore deserves special attention.

Here, we build a hydrogen evolution di-anionic surface on MoS₂ material to control its catalytic activity. Specifically, sulfur anions are electronically activated by heteroatom metal doping (Pd and Ru) to acquire optimized hydrogen adsorption energy. Meanwhile, –OH anions molecularly replace S sites at the interface in a controllable manner can create a reactant benign interface. The merits of the di-anion interface with –OH anion doping are: first, –OH functional groups attracts hydronium ions and water molecules closer to the inner Helmholtz plane (IHP) through hydrogen bonding, thus contributing to a reactant friendly interface; second, –OH sites work in conjunction with adjacent metal sites (M–OH) to split water in alkaline medium, thus enormously boosts the HER catalytic behavior. We show that the HER activity of the final catalyst exhibits highest kinetic performance exceeding the existed MoS₂ based material in both acidic and alkaline environments.

Results and discussion

Design for the di-anionic MoS_{2-x}(OH)_y. We initiate by conceiving –OH functional group as a perfect ligand for surface engineering, under the consideration that surface –OH groups can form hydrogen bonding with hydronium ions/water molecules and attract these reactants to the surface. Structurally, however, –OH introduction towards forming di-anionic surface without altering the phase structure is a grand challenge^{15–17}.

Fundamentally, a reaction needs to be both thermodynamically and kinetically favorable in order to occur at a distinctive rate. We design to circumvent these two challenges through a sequential element substitution strategy: first, thermodynamically, we dope MoS₂ with minor amount of Ru to make the substitution of S by –OH energetically favorable. The density functional theory (DFT) calculations reveal that the Ru-S bond energy (0.92 eV) is 0.87 eV lower than the Mo-S bond (1.79 eV), thus is more prone to form adjacent sulfur vacancies (Supplementary Fig. 1). Meanwhile, if Ru bonded defects sites are formed, they readily capture the nucleophilic –OH species owing to their thermodynamic favorable formation energies of –4.01 ~ –4.32 eV compared to other species (oxygen atom at –2.32 ~ –2.71 eV and O₂ at –1.02 ~ –1.41 eV) (Supplementary Fig. 2). Experimentally, the phenomenon that Ru is highly affinitive to OH has long been recognized and utilized in catalysis for a variety of reactions such as methanol oxidation and alkaline hydrogen oxidation (in PtRu), where Ru–OH is used as the co-catalyst for CO removal/water dissociation¹⁸. Second, kinetically, we trigger the Ru–S bond substitution by Ru–OH via surface redox reaction with Pd⁸. The Pd atomic doping, which occurs spontaneously at the interface to substitute Mo sites, kills two birds with one stone: (a) facilitates the formation of SVs at the energetically more favorable Ru adjacent sites, thus triggering further –OH anchoring to form stable Ru–OH bond (Supplementary Figs. 3, 4); (b) activates the Pd bonded sulfur atoms to exhibit optimal ΔG_{H^*} , as we have demonstrated recently⁸. Through this technique, it is expected that both ΔG_H and the concentration terms in Eq. 1 can be optimized via building a di-anionic surface.

Structural confirmation of the di-anionic MoS_{2-x}(OH)_y. Figure 1a and Supplementary Fig. 5 illustrated the synthetic procedures for the two-step doping strategy. In the first step, Ru-doped molybdenum disulfide (Ru-MoS₂) was synthesized via a typical one-pot hydrothermal synthesis technique (see Methods for the details). Ru-doped MoS₂ catalysts with Ru mass loadings of 1–15% were synthesized through tuning the Mo:Ru ratio in the precursors. X-ray diffraction (XRD), transmission electron microscopy (TEM) and scanning electron microscopy (SEM) patterns show the maintenance of the MoS₂ morphological and

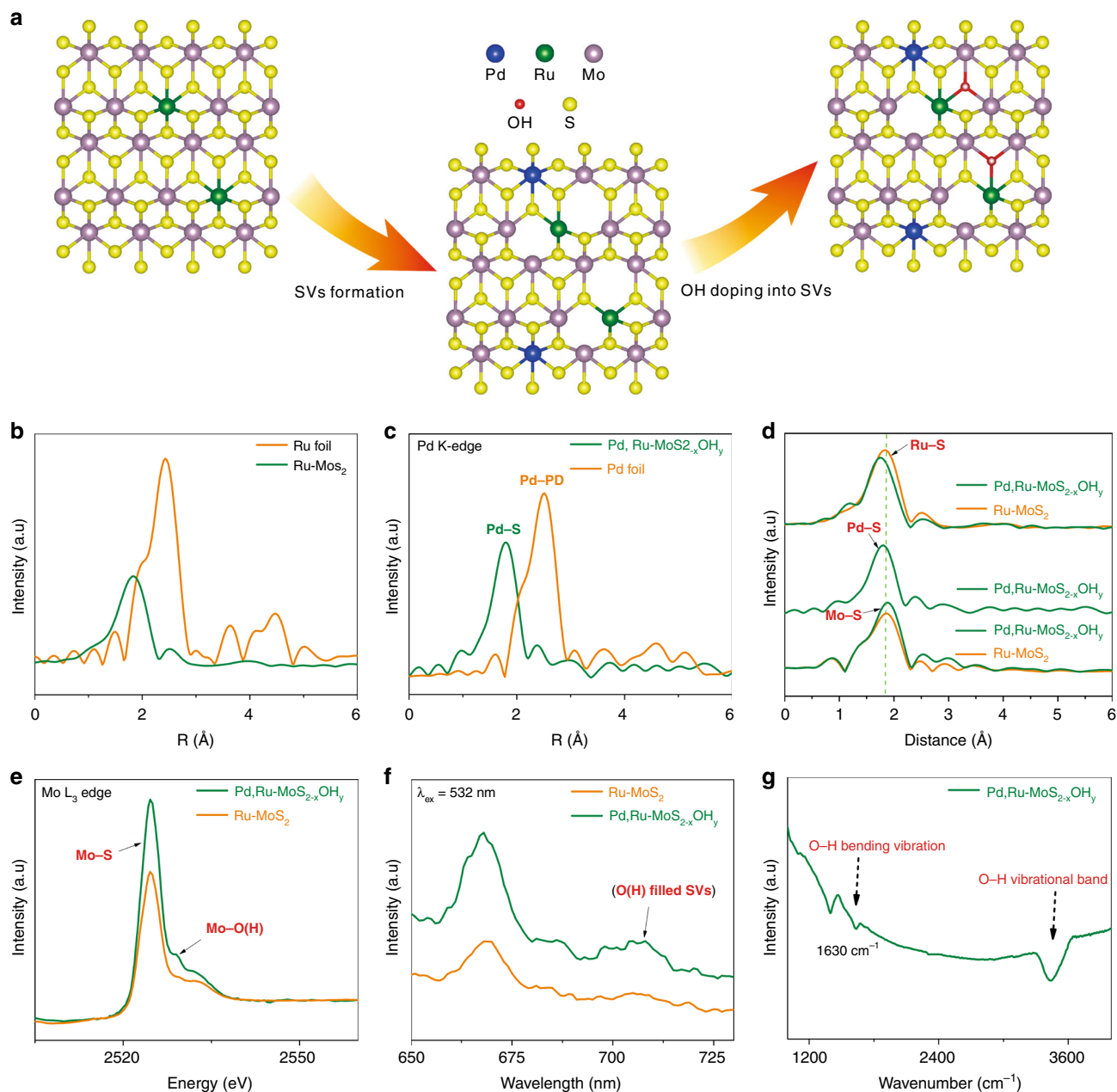


Fig. 1 Schematics for the O filled S vacancies (SVs). **a** Schematics for the synthesis strategy of Pd, Ru dual-doped MoS_{2-x}OH_y phase. Blue, yellow, purple, green and red spheres represent Pd, S, Mo, Ru, and O atoms, respectively. **b** Fourier transform of the k^2 -weighted Ru K-edge EXAFS spectra. **c** Fourier transform of the k^2 -weighted Pd K-edge of EXAFS spectra. **d** Fourier transform of the k^2 -weighted Pd K-edge, Ru K-edge and Mo K-edge EXAFS spectra. **e** Mo L₃-edge XANES spectra of Ru-MoS₂ and Pd, Ru-MoS_{2-x}OH_y. **f** Photoluminescence spectra of Ru-MoS₂ and Pd, Ru-MoS_{2-x}OH_y. **g** FTIR spectra of Pd, Ru-MoS_{2-x}OH_y.

crystal structure after Ru doping, until Ru doping content reaches 15% (Supplementary Figs. 6–8). Extended X-ray absorption fine structures (EXAFS) were measured to elucidate the Ru local bonding environment and the occupation sites in MoS₂, with 2.5% Ru-MoS₂ taken as a representative. The lack of Ru-Ru scattering path at 2.44 Å of Ru-MoS₂ in comparison with Ru foil verifies the atomic doping status of Ru. The Fourier transform (FT) of the k^2 -weighted Ru K-edge (Fig. 1b and Supplementary Fig. 9a) shows a notable peak at 1.75 Å, corresponding to a first shell Ru-S scattering path. The fitting result shows a Ru-S coordination number (CN) of 6.2 and Ru-S bond length at 2.33 Å (Supplementary Table 1), suggesting Ru atoms are saturatedly coordinated by S³.

In the second step, Pd was introduced to Ru-MoS₂ through a spontaneous interfacial redox strategy⁸, which is the key step for the formation of Ru adjacent SVs and the following -OH anchoring. The structure of the final material (Pd, Ru-MoS_{2-x}OH_y) was evaluated by SEM, TEM, XRD, Raman and sub-angstrom resolution aberration-corrected HAADF-STEM microscopy. SEM and TEM images (Supplementary Figs. 10, 11) show that Pd, Ru-MoS_{2-x}OH_y well retains the morphology of Ru-MoS₂ after Pd doping, where rose-like two-dimensional nanosheets are observed in both samples. Meanwhile, no nanoparticles or large clusters are observed in TEM image, thus ruling out the possibility of forming phase segregated palladium sulfide compounds, being consistent with the XRD patterns (Supplementary Fig. 12a). Raman spectra

(Supplementary Fig. 12b–c) of Pd, Ru–MoS_{2-x}OH_y show similar characteristics like the Ru–MoS₂. Furthermore, sub-angstrom resolution high angle annular dark field-scanning transmission electron microscopy (HAADF-STEM) images and the selected area electron diffraction (SAED) pattern (Supplementary Fig. 13) demonstrate the crystalline structure and the atomic dispersion of Pd in the final sample. Combining the above results together, it is suggested that the structure of the catalysts is well retained after Pd doping, where no obvious structure disorder occurs. The local chemical structure of Pd and Ru is further probed by EXAFS. The best fitting of *k*²-weighted Pd K-edge FT spectrum (Fig. 1c and Supplementary Fig. 14; Supplementary Table 2) shows similar profile and fitting parameters (Pd–S bond distance at 2.31 Å and CN = 3.9) to that of Mo (Mo–S bond distance at 2.30 Å and CN = 4.5) in MoS₂ (Supplementary Fig. 15; Supplementary Table 3), suggests that Pd substitute Mo or Ru atoms in Ru–MoS₂. Further evaluation of the final reactant solution (Supplementary Table. 4) by inductively coupled plasma mass spectrometry (ICP-MS) excludes the possibility of Pd to displace Ru sites, thus validating the atomic substitution of Mo by Pd. Of particular interesting is the Ru EXAFS spectrum (Fig. 1d) after Pd doping, where the nearest-neighbor FT Ru K-edge peak shows obvious shift towards the lower-R position, indicative the emerging of new bond with shorter scattering path¹⁹. The best fitting analyses clearly show that the path at 2.07 Å is satisfactorily interpreted as Ru–O(H) (the detailed structure of O containing species is not solved here, thus is denoted as –O(H)) contribution. The least-square EXAFS fitting analysis infer the Ru–S and Ru–O(H) coordination numbers of 4.5 (bond length 2.33 Å) and 1 (bond length 2.07 Å), respectively (Supplementary Fig. 9b; Supplementary Table 1). These results clearly demonstrate the incorporation of –O(H) to the sites adjacent to Ru. The decrease in overall Ru coordination number from 6.2 to 5.5 after Pd incorporation corroborates the net creation of Ru adjacent S vacancies in spite of the partial –O(H) refilling, in consistent with our DFT calculations (Supplementary Fig. 16 and Supplementary Discussion 1). If –O(H) sites are to replace the S atoms, additional Mo–O(H) should be noticed since –O(H) is to bound with two other adjacent Mo atoms. This is validated by the Mo K-edge EXAFS (Supplementary Fig. 17 and Table 5), where the coordination numbers of Mo–O(H) is found to be 0.3. Meanwhile, through X-ray absorption near-edge spectra (XANES) investigation, the presence of Mo–O(H) is directly confirmed with a shoulder peak observed at 2527 eV in the Mo L₃-edge (Fig. 1e). It is noted that only when Pd and Ru are co-doped through our technique results in the incorporation of the –O(H) into the MoS₂ substrate. The counterparts MoS₂ substrates, Ru–MoS₂, and Pd–MoS₂ were all examined through XAS, where no symbolic signals for –O(H) introduction were noticed.

The necessity of Pd, Ru dual doping for –O(H) incorporation is further verified by XPS, Raman and photoluminescence (PL) spectra. In Pd, Ru–MoS_{2-x}(OH)_y, O 1s peak corresponding to the binding energy of lattice oxygen is clearly observable at 530.5 eV (Supplementary Fig. 18a) in XPS spectra²⁰. On the contrary, the Ru–MoS₂ (Supplementary Fig. 18b) and the Pd–MoS₂ (Supplementary Fig. 18c) sample show the absence of the corresponding peak. In Raman spectra (Supplementary Fig. 19), a new signal around 283 cm⁻¹ is observed, attributable to B 2g mode of Mo–O(H) bonds¹³. In PL spectra (Fig. 1f), an obvious peak emerging at 710 nm (1.75 eV) is associated with the –O(H) filled S vacancies¹³, which again only appears when MoS₂ is double doped by Pd and Ru. To here, it is clear that Ru and Pd are both necessary for the –O(H) group introduction, in which the former makes the reaction thermodynamically favorable and the latter triggers the reaction kinetically via surface redox reaction.

We carried out the Fourier Transform infrared spectroscopy (FTIR) spectra and the proton solid-state nuclear magnetic resonance

(¹H SS-NMR) to further identify the oxygen-containing species in the catalysts. FTIR spectrum (Fig. 1g) of the Pd, Ru–MoS_{2-x}OH_y sample shows a strong signal of O–H vibrational bands, with a broad peak at 3000–3500 cm⁻¹ signifies the O–H bond stretching vibration and a peak at 1630 cm⁻¹ corresponds to O–H bending vibration^{21,22}. On the contrary, the MoS₂, Ru–MoS₂, and the Pd–MoS₂ sample show the absence of OH signature (Supplementary Fig. 20). Additionally, the ¹H NMR spectrum (Supplementary Fig. 21 and Supplementary discussion 2) of the Pd, Ru–MoS_{2-x}OH_y catalyst shows a peak at 2.802 ppm, which could match a hydrogen atom bonded to an oxygen atom²³. The counterparts MoS₂ substrates, Ru–MoS₂, and Pd–MoS₂ were all examined through ¹H SS-NMR spectrum, where no symbolic signals for –OH introduction were noticed. These results confirm our claim that the controlled molecular substitution of S by –OH sites was achieved by a sequential element substitution strategy. Thus, the final sample is unambiguously verified to represent a di-anionic MoS_{2-x}(OH)_y structure.

HER performance evaluation. Having established the successful creation of the di-anionic surface with molecular substitution of S sites by –OH, denoted as Pd, Ru–MoS_{2-x}(OH)_y, we turned to evaluate the final HER catalytic behavior of these different catalysts, started in acidic medium (Fig. 2a and Supplementary Figs. 22, 23). First, pristine MoS₂ shows an over potential of 10 mA cm⁻² (η @10 mA cm⁻²) at 355 mV, consistent with the values reported in literature^{24,25}. Second, Pd–MoS₂ and Ru–MoS₂ exhibit much higher activity than MoS₂ catalyst, respectively reaching over potentials of 10 mA cm⁻² (η @10 mA cm⁻²) at 201–128 mV (0.1–1 wt% Pd) and 170–140 mV (1–5 wt% Ru), mainly ascribable to the activation of in-plane S atoms^{8,26} (Supplementary Fig. 24). Third, the di-anionic Pd, Ru–MoS_{2-x}OH_y catalysts show even higher catalytic activities, especially in high current density region. Specifically, Pd, Ru–MoS_{2-x}OH_y (Ru: 2.5%, Pd: 0.5%) shows low overpotential of 45 and 93 mV to achieve 10 and 100 mA cm⁻² current density, respectively. This value, to the best of our knowledge, is the highest performance ever reported for MoS₂-based catalysts in acidic media^{7,13,27–30} (Supplementary Table. 6). Even more, supporting Pd, Ru–MoS_{2-x}OH_y catalyst on rGO substrate reinforces the catalytic activity to approach or even surpass that of Pt catalyst in high current density region (Supplementary Fig. 25). The superb activity of the Pd, Ru–MoS_{2-x}OH_y catalyst is likewise evidenced by its exchange current density (*i*₀), turnover frequency (TOF) (Supplementary Fig. 26; Table 7, Supplementary Note 1), and charge transfer resistance (R_{ct}) derived from electrochemical impedance spectroscopy (EIS) (Supplementary Fig. 27; Table 8). Although the *i*₀ and TOF of Pd, Ru–MoS_{2-x}OH_y is still below that of Pt^{31,32}, it is better than those of the best-characterized MoS₂-based materials^{6,33}.

The explicit role of –OH introduction in facilitating the HER catalytic activity is further verified by tuning the Pd content to control the –OH surface concentration. As monitored by XPS spectra (Fig. 2b and Supplementary Fig. 28; Table 9), the –OH content increases with the increase in Pd content, suggesting the essential role of Pd in introducing –OH functional group. We further plotted the current density (*J*) achieved at η = 140 mV as a function of Pd content in Pd, Ru–MoS_{2-x}OH_y (In Fig. 2c and Supplementary Fig. 29; Table 10). In all these samples, the content of Ru is fixed at 2.5 wt%, representing *J* of 7.58 mA cm⁻². The Pd–MoS₂ sample with differed Pd content was also plotted to offset the contribution from Pd. Fascinatingly, with the increase of –OH content in Pd, Ru–MoS_{2-x}OH_y, the performance gap between the two catalysts becomes more distinct. Specifically, the currents *J* (39.07–245.66 mA cm⁻²) of Pd, Ru–MoS_{2-x}OH_y (Pd doping content 0.1–1 wt%) outperforms the superimposed currents of the counterpart Pd–MoS₂ (0.1–1 wt%) samples

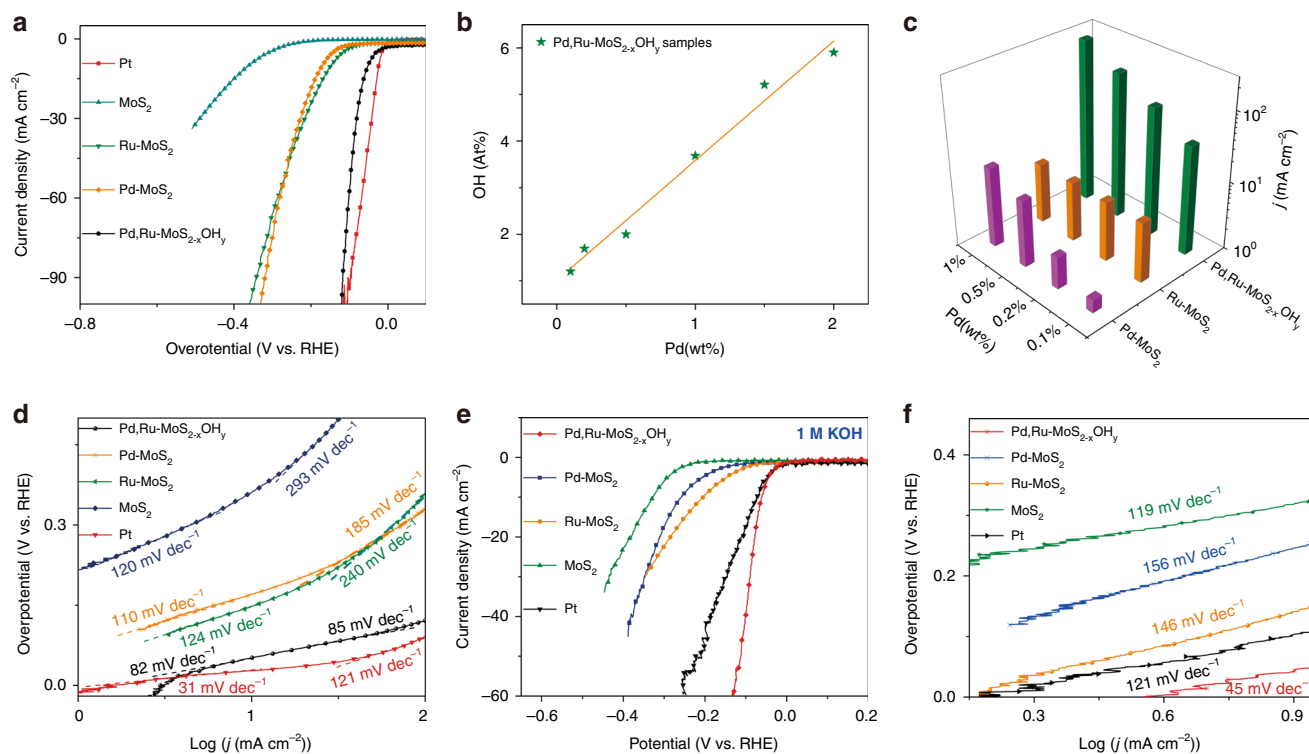


Fig. 2 Superior activity and stability of Pd, Ru-MoS_{2-x}OH_y. **a** LSV polarization curves of Pt, MoS₂, Ru-MoS₂, Pd-MoS₂ and Pd, Ru-MoS_{2-x}OH_y in 0.5 M H₂SO₄. (with *i*R correction). **b** OH content as a function of Pd content in Pd, Ru-MoS_{2-x}OH_y. **c** Current density achieved at $\eta = 140$ mV as a function of Pd content in Pd, Ru-MoS_{2-x}OH_y, Ru-MoS₂, and Pd-MoS₂. **d** Tafel plots derived from the results given in **a**. **e** LSV polarization curves of Pt, MoS₂, Ru-MoS₂, Pd-MoS₂ and Pd, Ru-MoS_{2-x}OH_y. (with *i*R correction) in 1 M KOH. **f** Tafel plots derived from the results given in **e**.

(1.55–14.94 mA cm⁻²) and Ru-MoS₂ (8.7 mA cm⁻²) by 29.94–223.14 mA cm⁻², where we attribute the net increase of 193.20 mA cm⁻² to the increase of the -OH content in the sample. We further support our argument through Tafel slope evaluation (Fig. 2d). In low current density region (within 1–10 mA cm⁻²), the Pd, Ru-MoS_{2-x}OH_y (82 mV dec⁻¹) exhibits much lower value than Pd-MoS₂ (110 mV dec⁻¹) and Ru-MoS₂ (124 mV dec⁻¹), possibly originated from both facilitation of the H* adsorption and double layer structure alternation induced by -OH. In high current density regions, the difference is more evident, where the mass transportation plays a more important role.^{34,35} Assuming that the di-anionic surface benefits the hydronium ion transfer, the much smaller Tafel slope (85 mV dec⁻¹) of Pd, Ru-MoS_{2-x}OH_y than the counterpart Pd-MoS₂ (185 mV dec⁻¹) and Ru-MoS₂ (240 mV dec⁻¹) is easily understandable.

It is apparent that HER in alkaline media is much more challenging than that in acidic media, due to the rigorous requirement for additional water dissociation.^{19,36,37} The corresponding HER polarization curves of all samples in 1 M KOH are illustrated in Fig. 2e. It is shown that the MoS₂ (-332 mV @ 10 mA cm⁻²), Ru-MoS₂ (-210 mV @ 10 mA cm⁻²) and Pd-MoS₂ (-260 mV @ 10 mA cm⁻²) electrodes indeed show limited catalytic performance in alkaline media due to the low water dissociation kinetics. In contrast, the Pd, Ru-MoS_{2-x}OH_y electrode ($\eta = 48$ mV @ 10 mA cm⁻², 131 mV @ 50 mA cm⁻²) shows a breakthrough in the catalytic activity, which far exceeds that of the Pt electrode ($\eta = 75$ mV @ 10 mA cm⁻², 218 mV @ 50 mA cm⁻²). This corresponds to the highest performance ever reported for MoS₂-based catalysts in alkaline media.^{10,38,39} The Pd, Ru-MoS_{2-x}OH_y catalyst also exhibits more than one magnitude increase in intrinsic activity, evidenced by its superior TOF (Supplementary Fig. 30). To

understand the origin of the differences in the overall catalytic performance between Pd, Ru-MoS_{2-x}OH_y, and counterpart Ru-MoS₂ electrodes, we estimated their relative electrochemically active surface areas using cyclic voltammetry measurements by extracting the double-layer capacitance (*C*_{dl}) (Supplementary Fig. 31). The relative electrochemical active surface areas for the Pd, Ru-MoS_{2-x}OH_y is similar to that of Ru-MoS₂, indicating that the higher catalytic activity of Pd, Ru-MoS_{2-x}OH_y achieved is not due to the increase in surface area. Tafel slope (Fig. 2f) evaluation clearly shows an alternation in reaction mechanism due to the -OH incorporation. Tafel slopes span over 140–160 mV dec⁻¹ for the pristine MoS₂, Ru-MoS₂, and Pd-MoS₂, signifying water discharge and formation of H* (Volmer reaction) as the rate-limiting step (RDS). Nevertheless, the Pd, Ru-MoS_{2-x}OH_y catalyst represents a Tafel slope at 45 mV dec⁻¹, suggesting the overcome of water dissociation barrier and the shift of RDS to the electrochemical desorption of hydrogen (the Heyrovsky step). Thus, we deduce that the exceptional alkaline HER activity of Pd, Ru-MoS_{2-x}OH_y is mainly aroused from the OH sites in attracting H₂O to the surface and the M-OH sites in facilitating the HO-H bond cleavage, considering Pd-MoS₂ and Ru-MoS₂ do not exhibit such activity.

We then carried out the long-term operating stability test, where the Pd, Ru-MoS_{2-x}OH_y show its very robust nature. Supplementary Fig. 32a, 33 show no observable decay during a 10 h test in both acidic and alkaline medium. The stability of the catalyst in acidic solution is primarily concerned, as the Ru-OH is suspicious to dissolution under the attack of hydronium ions. We therefore carried out a prolonged test for 100 h, where results show an overall decay of only 16 mV (Supplementary Fig. 32b), even comparable to the Pt based catalysts. (Supplementary Fig. 34, see the Supporting Information for details⁴⁰). The OH contents of Pd, Ru-MoS_{2-x}OH_y before and after were probed by XPS, and the values are not

obviously changed (Supplementary Fig. 35). Further, no leaching of Ru element in the electrolyte after tests was monitored. We conducted further XPS and (in situ) XANES investigations to examine the valence state of Ru the Pd, Ru-MoS_{2-x}OH_y sample after electrolysis. Notably, neither the content nor the valence state of Ru was altered for the post test sample according to the XPS, suggesting that Ru is firmly integrated into the MoS₂ backbone and highly stable under electrolytic conditions (Supplementary Fig. 36). Meanwhile, The Ru L₃-edge XANES results (Supplementary Fig. 37a) demonstrate no change in the white line resonance strength in comparison to the Pd, Ru-MoS_{2-x}OH_y sample before the electrolysis test, thereby suggesting that the average valence of Ru sites is not changed. More importantly, operando X-ray absorption near-edge structure (XANES) provides the most direct evidence to unveil that Ru is not reduced under HER conditions. Supplementary Fig. 38a, b presents the operando XANES spectra at the Ru K-edge of the Pd, Ru-MoS_{2-x}OH_y catalyst recorded at different applied potentials. The ex-situ sample, the sample at open-circuit potential, and the ones under cathodic potentials between 0 and -0.05 V all show similar absorption edge, suggesting that Ru maintains its +3 valence state during HER process. Meanwhile, the first derivative of the adsorption edge shows no variation in intensity maximum, thus further suggesting the unaltered valence state of Ru during HER. This result clearly demonstrates that the Ru-OH is stably introduced, where the -OH is chemical stabilized by 1 Ru and 2 Mo atoms and Ru is stabilized by an overall 5.5 covalent S/OH bonds. Further, the post XPS and XANES results (Supplementary Figs. 37b, 39) of the Pd, Ru-MoS_{2-x}OH_y sample after electrolysis reveal that Pd is also firmly integrated into the MoS₂ backbone and highly stable under electrolytic conditions. Operando XANES spectra (Supplementary Fig. 38c, d) of the Pd K-edge shows no shift of the absorption energy edge of the Pd, Ru-MoS_{2-x}OH_y between in situ and ex situ sample, thus implying that no change in the Pd average valence state occurs during the HER process.

Fundamental understanding of the di-anionic effect. Up to this point, we have demonstrated that di-anionic surface vastly promotes the HER activity in both acidic and alkaline medium. In what follows, we try to obtain fundamental understanding of the di-anionic effect using a combination of theoretical and experimental techniques. We have demonstrated in a previous paper that the Pd bonded S* exhibit ΔG_{H} at -0.02 eV⁸, which shows optimized chemical adsorption behavior. (see Supplementary Note 2 for details and Supplementary Fig. 36–41). Therefore, we here focus on the effect of -OH part for further performance enhancement. First, we computed interaction between H⁺(H₂O)_n and the surface -OH sites using density functional theoretical calculations. The projected density of states (pDOS) (Supplementary Fig. 42) were performed to study the bonding and electronic structure between -OH and H₂O. The delocalized molecular orbitals of O adsorbed on Pd, Ru-MoS_{2-x}OH_y interact weakly with the H 1s orbital in the -9.2 to -9.0 eV energy zone, thus confirms the presence of the non-covalent bonding^{41,42}. We then carried out electron localization function (ELF) evaluations (Fig. 3a) to measure the excess kinetic energy density due to the Pauli repulsion⁴¹. The topological image shows that the V(O, H) basin belongs to the OH in Pd, Ru-MoS_{2-x}OH_y valence shell sharing a boundary with V(O) basin, typical for hydrogen bonding^{43–45}. Further energy evaluation (Fig. 3b) shows a stabilization energy of 58 kJ mol⁻¹ (0.58 eV), indicates a hydrogen bonding that is even stronger than the inter-molecular HB energy in water (42 kJ mol⁻¹, 0.42 eV)¹¹. Thus, the hydronium ions and water molecules (Supplementary Fig. 43 and Supplementary discussion 3) are more easily dragged to the catalyst surface due

to the energy preference. Second, we used Bader charge analysis (Fig. 3c) to understand the reason for the formation of stronger HB. We found -OH sites display strong acceptor-type behavior, characterized by -1.12 e negative charge, almost three times higher than the charge on S atoms (-0.37 ~ -0.58 e)¹³. Moreover, the presence of OH sites brings about local charge redistribution, where the electrons in the MoS₂ backbone are drawn to -OH and its adjacent site, thus enormously facilitates the formation of stronger hydrogen bonding due to this electron transfer process. This is more clearly reflected in charge density difference evaluation (Supplementary Fig. 44), where the localized negative charge is obviously focused on OH group and its nearby S atoms²². Third, the hydrogen bonding formation is probed experimentally by the contact angle and the potential of zero charge (PZC) evaluations. Macroscopically, the Pd-MoS₂ and Ru-MoS₂ samples show contact angles at 125° and 130°, clearly demonstrate their water repelling feature. The Pd, Ru-MoS_{2-x}OH_y di-anionic surface, on the contrary, shows a water withdrawing feature with a contact angle of 75° (Supplementary Fig. 45). This is further reflected in E_{PZC} (Fig. 3d), where the more polarized Pd, Ru-MoS_{2-x}(OH)_y surface represents a much more positive value at 0.550 V vs. RHE in comparison to its counterpart MoS₂ (0.095 V), Ru-MoS₂ (0.102 V), and Pd-MoS₂ (0.318 V)⁴⁶. Thus, the electrode has a strong tendency to drag hydronium ions to its surface and transfer electrons to the reactant, with a lower work function (3.22 eV in comparison to 3.82 eV) confirmed by the ultraviolet photoelectron spectroscopy (UPS)²⁶ (Supplementary Fig. 46).

The aid of -OH functionality in promoting HER on the di-anionic MoS_{2-x}(OH)_y electrode is then proposed in Fig. 4. Without the -OH functionalities, water or hydronium ions are located at the outer Helmholtz plane (OHP) in its clustered structure (Fig. 4a). Thus, extra polarization energy is necessitated to counter balance the HB and brings the reactant from OHP to IHP. In terms of di-anionic MoS_{2-x}(OH)_y electrode, however, with much stronger HB formed, water/hydronium ions are preferentially attracted to IHP and leads to further reaction (Fig. 4b, step I₁ and step I₂). In acidic solution, the protons migrate to the energetically preferred Pd-S* sites (step II₁) (the asterisk denotes the adsorption site) and are reduced by one electron to produce Pd-S*-H (step III₁) (see Supplementary Note 2 for details)⁸. Finally, another proton from an adjacent H⁺(H₂O)_n reacts with the first H_{ad} to generate H₂ (step IV₁-V₁), in a Heyrovsky mechanism. In alkaline medium, we seek the mechanistic origin for the overcome of water dissociation kinetic barriers. At the Ru-OH site, while -OH attracts water to the surface, we propose that the splitting of water occurs at the Ru site, as shown in step II₂. This is supported by the appropriate ΔE_{OH} (-2.8 ~ -2.54 eV) to a second -OH site at the Ru adjacent S vacancy (Supplementary Fig. 47). The moderate ΔE_{OH} leads to an easy HO-H bond cleavage with formation of adsorbed H* and Ru-(OH)₂, followed by the removal of the second -OH site to its original structure (step III₃)^{47,48}. Therefore, it is believed that OH works in conjunction with adjacent Ru (Ru-OH) to overcome the water dissociation kinetic barrier⁴⁹. We then carried out further experiments to verify the synergistic role of the M-OH (M = Ni, Co) in activating water in the basal plane of MoS₂ (see Supplementary Note 3 for details and Supplementary Figs. 48–51). The transition of RDS away from Volmer to Heyrovsky step is noticed in all other catalysts, further verifying that metal sites and -OH groups work coordinately to surmount the water dissociation barrier.

In summary, we confirm the essential role of reactant friendly interface for kinetic advancement of HER, through constructing a di-anionic surface (S and -OH) on MoS₂. The controlled molecular

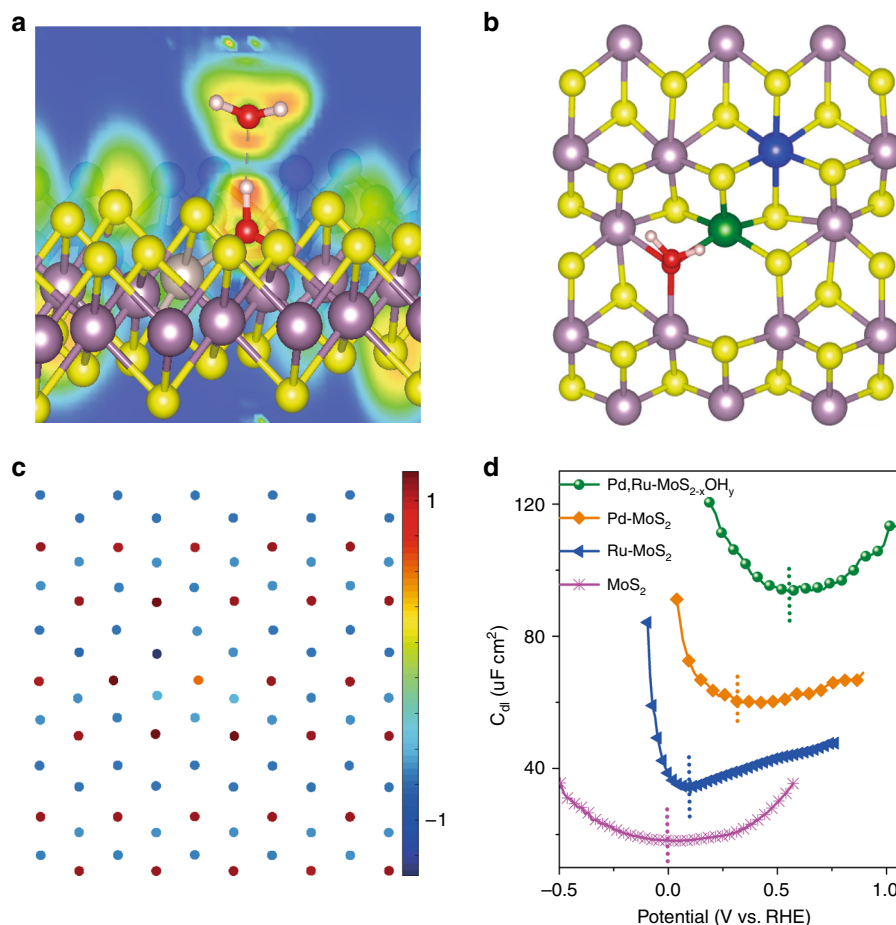


Fig. 3 Using theoretical and experimental techniques to understanding the di-anionic effect. **a** Electron localization function (ELF) evaluations. **b** Interaction energy between H₂O and the surface -OH sites. **c** Bader charge analysis. **d** E_{pzc} measured for Pd, Ru-MoS_{2-x}OH_y, Ru-MoS₂, Pd-MoS₂, and MoS₂.

substitution of S by -OH sites was achieved by a sequential element substitution strategy and confirmed by a combination of various techniques. The -OH groups were revealed to form strong non-covalent hydrogen bonding (56 kJ mol⁻¹) to the reactants, thereby attracting the reactants (hydronium ions and water molecules) closer to the inner Helmholtz plane (IHP). Besides, the di-anionic surface is endowed with a water dissociation feature to surmount the Volmer reaction barriers (in alkaline media). Excitingly, the final di-anionic MoS_{2-x}(OH)_y exhibits highest kinetic performance among the existed MoS₂ based materials, which is even comparable to (in acid) or better than (in alkaline) the state-of-the-art platinum catalysts, accompanied with outstanding long-term operation stability beyond 100 h. Our work provides a direction for manipulating catalytic properties beyond MoS₂ and for heterogeneous catalysis beyond HER via designing catalytic interfaces that are reactants benign.

Methods

Materials synthesis. The Ru-MoS₂ material was synthesized through a solvothermal method. Firstly, 0.538 g of sodium molybdate (Na₂MoO₄·2H₂O), 0.6 g of thiourea (CH₄N₂S) and 1.094 ml RuCl₃ (11.082 mg ml⁻¹) were dissolved in 23.906 ml of water in a beaker and then sonicated for 30 min. The resulting homogenous solution was transferred into a 50 ml Teflon-lined stainless-steel autoclave and heated to 200 °C for 24 h. After cooling to room temperature, the precipitate was separated by centrifugation and washed with methanol and finally dried at 50 °C for overnight. The Pd, Ru-MoS_{2-x}OH_y catalyst was synthesized as follows. Sixty milligram of Ru-MoS₂ powder was mixed with 50 ml H₂O in a round-bottom flask, and the mixture was ultrasonicated for 1 h; then the Pd (OAc)₂ solution was added and heated to 90 °C for 12 h. The obtained product was obtained by filtration of the suspension, followed by dialysis in deionized water.

Materials characterization. Ru and Pd K-edge X-ray absorption spectra were performed at the BL14W1 beamline of the Shanghai Synchrotron Radiation Facility, operating at 3.5 GeV with injection currents of 140–210 mA. Si (111) and Si (311) double-crystal monochromators were used to reduce the harmonic component of the monochrome beam. The Ru L₃-edge XANES spectra were tested at the 4B7A beamline of the Beijing Synchrotron Radiation Facility (BSRF), China, in total electron yield (TEY) mode, where the sample drain current was collected under pressure smaller than 5 × 10⁻⁸ Pa. while Pd L₃-edge spectra were measured by partial fluorescence yield (PFY) mode with a SDD detector vertical to incident monochromatic X-ray. The beam from a bending magnet was monochromatic with a varied line-spacing plane grating and was refocused by a toroidal mirror. The photoluminescence (PL) spectra were performed at room temperature under ambient conditions, using a 532 nm excitation laser. X-ray photoelectron spectroscopy (XPS) measurements were carried out on Mg Kα radiation source (Kratos XSAM-800 spectrometer). The bulk compositions were evaluated by inductively coupled plasma optical emission spectrometer (X Series 2, Thermo Scientific USA). Nuclear magnetic resonance (NMR) measurements were carried out using a Bruker Avance III 500 MHz spectrometer which was equipped with a double tuned 4 mm MAS probe. Transmission electron microscopy (TEM), high resolution transmission electron microscopy (HRTEM), high-annular dark-field scanning transmission electron microscopy (STEM), and element mapping analysis were conducted on Philips TECNAI G2 electron microscope operating at 200 kV. FTIR spectra were collected using a Nicolet 8700 infrared spectrometer with a resolution of 4 cm⁻¹. All samples were mixed with KBr (Sigma-Aldrich) by grinding before being pressed into pellets.

Electrochemical measurements. All electrochemical measurements were carried out in a N₂-saturated H₂SO₄ solution (0.5 M) standard three-electrode setup using Princeton Applied Research. Inks were prepared by ultrasonically dispersing 5 mg of the samples in a suspension containing 50 μl of a Nafion (5 wt%) solution and 950 μl ethanol. The catalysts loading were calculated as approximately 0.357 mg cm⁻². The HER performances were performed in N₂-saturated 0.5 M H₂SO₄ using the linear sweep voltammetry at a scan rate of 5 mV s⁻¹. All data presented were *iR* corrected,

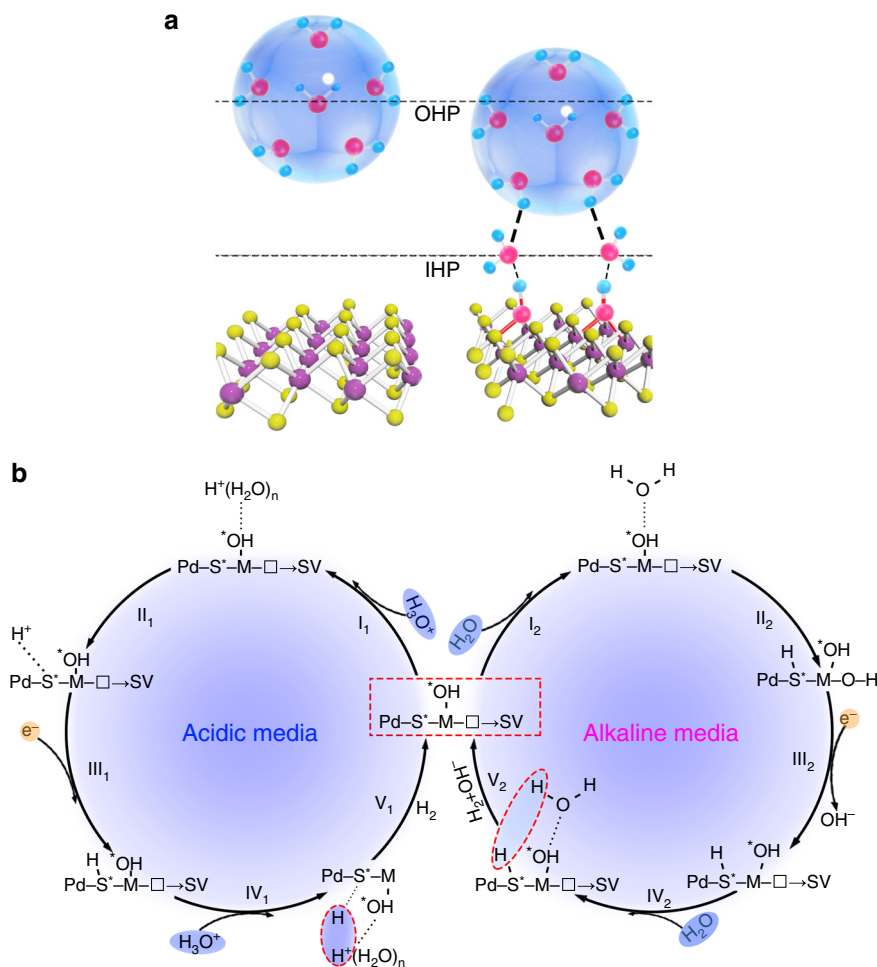


Fig. 4 Correlation of the HER mechanism with the different reaction condition. **a** Schematic illustration of OH functionality in promoting HER on the di-anionic $\text{MoS}_{2-x}(\text{OH})_y$ electrode through forming strong non-covalent hydrogen bonding to the reactants (hydronium ions or water). **b** Left: HER mechanism of Pd, Ru- $\text{MoS}_{2-x}\text{OH}_y$ in acidic media; Right: HER mechanism of Pd, Ru- $\text{MoS}_{2-x}\text{OH}_y$ in alkaline media.

where the solution resistances were determined by EIS experiments. The potential values shown were calibrated vs. the reversible hydrogen electrode (RHE).

DFT calculations. Vienna ab initio simulation package of DFT performed accurate to describe the calculated models⁵⁰. The interactions between valence electrons and frozen cores were described by the projected augmented wave method⁴⁹. The GGA method as implemented with Perdew, Burke, and Ernzerhof function⁵¹ was used to describe the exchange-correlation functional component of the Hamiltonian. The kinetic energy cutoff was 400 eV for the plane-wave expansion. To sample the Brillouin zone, the calculation used Monkhorst-Pack $3 \times 3 \times 1$ k-point meshes for structure relaxation and $5 \times 5 \times 1$ k-point grid for the exploration of electronic properties⁵². The geometry convergence tolerance for energy change, max force was 1×10^{-4} eV and 0.01 eV \AA^{-1} , respectively. When building models of different configurations, a large vacuum space of 16 Å was employed to avoid the interactions between MoS_2 layers.

Data availability

The data that support the findings of this study are available from the authors on reasonable request; see author contributions for specific data sets.

Received: 31 July 2019; Accepted: 11 February 2020;

Published online: 28 February 2020

References

- Karunadasa, H. I. et al. A molecular MoS_2 edge site mimic for catalytic hydrogen generation. *Science* **335**, 698–702 (2012).

- Kibsgaard, J., Chen, Z. B., Reinecke, B. N. & Jaramillo, T. F. Engineering the surface structure of MoS_2 to preferentially expose active edge sites for electrocatalysis. *Nat. Mater.* **11**, 963–969 (2012).
- Zhang, G., Liu, H., Qu, J. & Li, J. Two-dimensional layered MoS_2 : rational design, properties and electrochemical applications. *Energy Environ. Sci.* **9**, 1190–1209 (2016).
- Koper, M. T. M. Activity volcanoes for the electrocatalysis of homolytic and heterolytic hydrogen evolution. *J. Solid State Electr.* **20**, 895–899 (2016).
- Koper, M. T. M. Analysis of electrocatalytic reaction schemes: distinction between rate-determining and potential-determining steps. *J. Solid State Electr.* **17**, 339–344 (2013).
- Wang, Q. et al. Design of active nickel single-atom decorated MoS_2 as a pH-universal catalyst for hydrogen evolution reaction. *Nano Energy* **53**, 458–467 (2018).
- Gao, M. R. et al. An efficient molybdenum disulfide/cobalt diselenide hybrid catalyst for electrochemical hydrogen generation. *Nat. Commun.* **6**, 5982 (2015).
- Luo, Z. et al. Chemically activating MoS_2 via spontaneous atomic palladium interfacial doping towards efficient hydrogen evolution. *Nat. Commun.* **9**, 2120 (2018).
- Strmcnik, D. et al. Enhanced electrocatalysis of the oxygen reduction reaction based on patterning of platinum surfaces with cyanide. *Nat. Chem.* **2**, 880–885 (2010).
- Zhang, J. et al. Interface engineering of $\text{MoS}_2/\text{Ni}_3\text{S}_2$ heterostructures for highly enhanced electrochemical overall-water-splitting activity. *Angew. Chem. Int. Ed.* **55**, 6702–6707 (2016).
- Strmcnik, D. et al. The role of non-covalent interactions in electrocatalytic fuel-cell reactions on platinum. *Nat. Chem.* **1**, 466–472 (2009).
- Ledezma-Yanez, I. et al. Interfacial water reorganization as a pH-dependent descriptor of the hydrogen evolution rate on platinum electrodes. *Nat. Energy* **2**, 110 (2017).

13. Peto, J. et al. Spontaneous doping of the basal plane of MoS₂ single layers through oxygen substitution under ambient conditions. *Nat. Chem.* **10**, 1246–1251 (2018).
14. Barja, S. et al. Identifying substitutional oxygen as a prolific point defect in monolayer transition metal dichalcogenides. *Nat. Commun.* **10**, 3382 (2019).
15. Li, Y. F., Zhou, Z., Zhang, S. B. & Chen, Z. F. MoS₂ nanoribbons: high stability and unusual electronic and magnetic properties. *J. Am. Chem. Soc.* **130**, 16739–16744 (2008).
16. Gronborg, S. S. et al. Synthesis of epitaxial single-layer MoS₂ on Au(111). *Langmuir* **31**, 9700–9706 (2015).
17. Kc, S., Longo, R. C., Wallace, R. M. & Cho, K. Surface oxidation energetics and kinetics in MoS₂ monolayer. *J. Appl. Phys.* **117**, 135301 (2015).
18. Gómez de la Fuente, J. L. et al. Tailoring and structure of PtRu nanoparticles supported on functionalized carbon for DMFC applications: new evidence of the hydrous ruthenium oxide phase. *Appl. Catal. B* **88**, 505–514 (2009).
19. Dinh, C. T. et al. Multi-site electrocatalysts for hydrogen evolution in neutral media by destabilization of water molecules. *Nat. Energy* **4**, 107–114 (2019).
20. Wang, B. B. et al. Structure and photoluminescence properties of MoO_{3-x}/graphene nanoflake hybrid nanomaterials formed via surface growth. *Appl. Surf. Sci.* **480**, 1054–1062 (2019).
21. Whittaker, T. et al. H₂ Oxidation over supported Au nanoparticle catalysts: evidence for heterolytic H₂ activation at the metal-support interface. *J. Am. Chem. Soc.* **140**, 16469–16487 (2018).
22. Cao, L. L. et al. Identification of single-atom active sites in carbon-based cobalt catalysts during electrocatalytic hydrogen evolution. *Nat. Catal.* **2**, 134–141 (2019).
23. Rimsza, J. M., Sorte, E. G. & Alam, T. M. Hydration and hydroxylation of MgO in solution: NMR identification of proton-containing intermediate phases. *ACS Omega* **4**, 1033–1044 (2019).
24. Li, G. et al. All the catalytic active sites of MoS₂ for hydrogen evolution. *J. Am. Chem. Soc.* **138**, 16632–16638 (2016).
25. Deng, J. et al. Triggering the electrocatalytic hydrogen evolution activity of the inert two-dimensional MoS₂ surface via single-atom metal doping. *Energy Environ. Sci.* **8**, 1594–1601 (2015).
26. Shi, Y. et al. Energy level engineering of MoS₂ by transition-metal doping for accelerating hydrogen evolution reaction. *J. Am. Chem. Soc.* **139**, 15479–15485 (2017).
27. Voiry, D. et al. The role of electronic coupling between substrate and 2D MoS₂ nanosheets in electrocatalytic production of hydrogen. *Nat. Mater.* **15**, 1003–1009 (2016).
28. Nayak, A. P. et al. Pressure-induced semiconducting to metallic transition in multilayered molybdenum disulfide. *Nat. Commun.* **5**, 3731 (2014).
29. Zhang, Z. et al. Hierarchical composite structure of few-layers MoS₂ nanosheets supported by vertical graphene on carbon cloth for high-performance hydrogen evolution reaction. *Nano Energy* **18**, 196–204 (2015).
30. Zhang, X., Li, L., Guo, Y., Liu, D. & You, T. Amorphous flower-like molybdenum-sulfide-@-nitrogen-doped-carbon-nanofiber film for use in the hydrogen-evolution reaction. *J. Colloid Interface Sci.* **472**, 69–75 (2016).
31. Zheng, J., Yan, Y. & Xu, B. Correcting the hydrogen diffusion limitation in rotating disk electrode measurements of hydrogen evolution reaction kinetics. *J. Electrochem. Soc.* **162**, F1470–F1481 (2015).
32. Sheng, W., Gasteiger, H. A. & Shao-Horn, Y. Hydrogen oxidation and evolution reaction kinetics on platinum: acid vs. alkaline electrolytes. *J. Electrochem. Soc.* **157**, B1529 (2010).
33. Li, H. et al. Corrigendum: activating and optimizing MoS₂ basal planes for hydrogen evolution through the formation of strained sulphur vacancies. *Nat. Mater.* **15**, 364 (2016).
34. Feng, J. X., Tong, S. Y., Tong, Y. X. & Li, G. R. Pt-like hydrogen evolution electrocatalysis on PANI/CoP hybrid nanowires by weakening the shackles of hydrogen ions on the surfaces of catalysts. *J. Am. Chem. Soc.* **140**, 5118–5126 (2018).
35. Yu, X. et al. “Superaerophobic” nickel phosphide nanoarraycatalyst for efficient hydrogen evolution at ultrahigh current densities. *J. Am. Chem. Soc.* **141**, 7537–7543 (2019).
36. Luo, Y. T. et al. Morphology and surface chemistry engineering toward pH-universal catalysts for hydrogen evolution at high current density. *Nat. Commun.* **10**, 269 (2019).
37. Zang, Y. P. et al. Tuning orbital orientation endows molybdenum disulfide with exceptional alkaline hydrogen evolution capability. *Nat. Commun.* **10**, 1217 (2019).
38. Staszak-Jirkovsky, J. et al. Design of active and stable Co-Mo-Sx chalcogenides as pH-universal catalysts for the hydrogen evolution reaction. *Nat. Mater.* **15**, 197–203 (2016).
39. Zhang, B. et al. Interface engineering: the Ni(OH)₂/MoS₂ heterostructure for highly efficient alkaline hydrogen evolution. *Nano Energy* **37**, 74–80 (2017).
40. El-Sayed, H. A., Weiß, A., Olbrich, L. F., Putro, G. P. & Gasteiger, H. A. OER catalyst stability investigation using RDE technique: a stability measure or an artifact? *J. Electrochem. Soc.* **166**, F458–F464 (2019).
41. Farias, S. A. S. & Martins, J. B. L. Bonding and electronic structure of sillenites. *Chem. Phys. Lett.* **533**, 78–81 (2012).
42. Lin, L. et al. A highly CO-tolerant atomically dispersed Pt catalyst for chemoselective hydrogenation. *Nat. Nanotechnol.* **14**, 354–361 (2019).
43. Alikhani, M. E., Fuster, F. & Silvi, B. What can tell the topological analysis of ELF on hydrogen bonding? *Struct. Chem.* **16**, 203–210 (2005).
44. Grabowski, S. J. What is the covalency of hydrogen bonding? *Chem. Rev.* **111**, 2597–2625 (2011).
45. Fuster, F. & Silvi, B. Does the topological approach characterize the hydrogen bond? *Theor. Chem. Acc.* **104**, 13–21 (2000).
46. Choi, C. H. et al. The Achilles’ heel of iron-based catalysts during oxygen reduction in an acidic medium. *Energy Environ. Sci.* **11**, 3176–3182 (2018).
47. Subbaraman, R. et al. Trends in activity for the water electrolyser reactions on 3d M(Ni,Co,Fe,Mn) hydr(oxy)oxide catalysts. *Nat. Mater.* **11**, 550–557 (2012).
48. Farinazzo Bergamo Dias Martins, P. et al. Hydrogen evolution reaction on copper: Promoting water dissociation by tuning the surface oxophilicity. *Electrochem. Commun.* **100**, 30–33 (2019).
49. Kresse, G. & Joubert, D. From ultrasoft pseudopotentials to the projector augmented-wave method. *Phys. Rev. B* **59**, 1758–1775 (1999).
50. Kresse, G. & Furthmüller, J. Efficiency of ab-initio total energy calculations for metals and semiconductors using a plane-wave basis set. *Comput. Mater. Sci.* **6**, 15–50 (1996).
51. Zhang, Y. K. & Yang, W. T. Comment on “Generalized gradient approximation made simple”. *Phys. Rev. Lett.* **80**, 890–890 (1998).
52. Evarestov, R. A. & Smirnov, V. P. Modification of the Monkhorst-Pack special points meshes in the Brillouin zone for density functional theory and Hartree-Fock calculations. *Phys. Rev. B* **70**, 11 (2004).

Acknowledgements

The work is supported by the National Key R&D Program of China (2018YFB1502400), the National Natural Science Foundation of China (21633008), the Strategic Priority Research Program of CAS (XDA 21090400), Jilin Province Science and Technology Development Program (20190201300JC). Prof. Wei Xing thanks Gusu talent program for the financial support.

Author contributions

J.G. and Z. Jiang co-supervised the whole work. Z.L., Y.L., and Z. Jin contributed to the synthesis of material and the characterization. Z.L., X.W., Y.L., W.X., J.G., and C.L. contributed to analysis of the electrochemical experiments results. Y.Y. and Z. Jiang contributed to the theory calculation. H.Z. and Z. Jiang contributed to the X-ray absorption fine structure spectroscopy and total electron yield spectroscopy. The manuscript was primarily written by Z.L., J.G., and Z. Jiang. All authors contributed to discussions and manuscript review.

Competing interests

The authors declare no competing interests.

Additional information

Supplementary information is available for this paper at <https://doi.org/10.1038/s41467-020-14980-z>.

Correspondence and requests for materials should be addressed to Z.J. or J.G.

Reprints and permission information is available at <http://www.nature.com/reprints>

Publisher’s note Springer Nature remains neutral with regard to jurisdictional claims in published maps and institutional affiliations.



Open Access This article is licensed under a Creative Commons Attribution 4.0 International License, which permits use, sharing, adaptation, distribution and reproduction in any medium or format, as long as you give appropriate credit to the original author(s) and the source, provide a link to the Creative Commons licence, and indicate if changes were made. The images or other third party material in this article are included in the article’s Creative Commons licence, unless indicated otherwise in a credit line to the material. If material is not included in the article’s Creative Commons licence and your intended use is not permitted by statutory regulation or exceeds the permitted use, you will need to obtain permission directly from the copyright holder. To view a copy of this licence, visit <http://creativecommons.org/licenses/by/4.0/>.

© The Author(s) 2020